Vector coupled-wave analysis of hemispherical grid gratings for visible light

2004 J. Opt. A: Pure Appl. Opt. 6 384

(http://iopscience.iop.org/1464-4258/6/4/014)

INSTITUTE OF PHYSICS PUBLISHING JOURNAL OF OPTICS A: PURE AND APPLIED OPTICS

J. Opt. A: Pure Appl. Opt. **6** (2004) 384–389 PII: S1464-4258(04)70420-1

Vector coupled-wave analysis of hemispherical grid gratings for visible light

ZhiBin Ren and ZhenWu Lu

State Key Laboratory of Applied Optics, Changchun Institute of Optics, Fine Mechanics and Physics, Chinese Academy of Sciences, Changchun 130033, People's Republic of China

E-mail: ren_zb@yahoo.com.cn and Luzw@sklao.ac.cn

Received 10 October 2003, accepted for publication 10 February 2004
Published 12 March 2004
Online at stacks.iop.org/JOptA/6/384 (DOI: 10.1088/1464-4258/6/4/014)

Abstract
With the rapid development of modern science, the techniques of fabricating two-dimensional surface-relief gratings with a hemispherical grid for visible light by chemical methods are proving to be successful. In this paper, we use a multi-level structure to simulate this kind of grating and adopt the Lagrange multiplier method to minimize the volume error, and the rigorous coupled-wave method is employed to analyse the vector diffraction properties of this kind of grating. By computer simulation and calculation, the relations between the reflectivity and the structure parameters of the gratings are presented, and the antireflective characteristics are also studied when visible light is incident upon them. The results show that this kind of grating is capable of reducing reflections, and could achieve very low reflectivity over a wide field of view and a wide waveband by choosing appropriate parameters. The results also show that the errors can be neglected when $L \geqslant 16$ and the results are proved to be credible.

Keywords: hemispherical grid subwavelength gratings, rigorous coupled-wave analysis, antireflection, diffractive optics

1. Introduction

It is well known that conventional multi-layered thin-films are often used for antireflective coatings. There are, however, only a handful of optical materials available, thus limiting the performance that could ideally be achieved. On the other hand, subwavelength structure (SWS) surfaces, which are surface-relief gratings with periods smaller than the incident wavelength, have been researched and found to have antireflective properties [1–6]. By etching a binary subwavelength grating onto the surface of a material, one can synthesize an artificial thin film, which is more stable than the multi-layered thin-film coating since it is fabricated from a single material. Until now, the pattern generated by electron beam lithography or laser holographic recording have been transferred to the surface by replication or reactive ion etching [7–16]. In these exposure and transferring methods, however, the SWS surface grating to be designed over the visible light waveband is not always fabricated easily and it consumes a lot of time. Recently, monolayer colloidal spherical microparticle arrays have been fabricated through chemical methods, whose diameters range from 0.02 to 10 μm [17]. Moreover, colloidal stamps, which are the duplicate negatives of the microparticle arrays, have been made and the hemispherical subwavelength surface relief gratings could be generated by transferring the surface shape of the colloidal stamps onto the surface of optical elements [18–20]. As this kind of grating can be fabricated easily and perfectly and can be duplicated by using a sol–gel method which can produce a glass SWS on a glass substrate, they could behave as antireflective surfaces for visible light.

However, as we know, there have been no theoretical studies on the hemispherical subwavelength surface relief gratings shown in figure 1. In this paper we use the rigorous coupled-wave method to analyse and calculate the characteristics of the hemispherical grid grating, which is

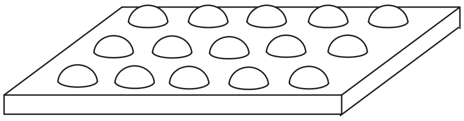

Figure 1. A two-dimensional surface-relief grating with hemispherical grid.

approximated by the multi-level columned structure shown in figure 2. The results show that this kind of grating is capable of reducing reflections and we can get very low reflectivity by choosing appropriate parameters. Fortunately, the results satisfy energy conservation, and the numerical instability problem and the convergence problem have not emerged in our calculations.

2. Description of the theory

A two-dimensional surface-relief grating with hemisphere profile with radius $\boldsymbol{R}$ is shown in figure 1. To study the optical characteristics of the grating, we may use a multi-step column structure which is shown in figure 2 to simulate it. We could assume that the diameter of the hemisphere $\boldsymbol{D}$ to be equal to $2\boldsymbol{R}$, $\boldsymbol{T}$ to be equal to the period of the grating, the depth of the lth level to be h_l and the radius of the lth level to be r_l.

In figure 2, however, there is an error when we use the multi-step column structure to simulate the hemisphere. To minimize the error, we should choose appropriate values of h_l to make sure the volume of the multi-step structure (V_m) approximates the volume of the hemisphere (V_h). The volume error $E(h_1, h_2, \ldots, h_L)$ can be expressed as

$$E(h_1, h_2, \ldots, h_L) = V_m - V_h = \sum_{i=1}^{L} \pi r_i^2 h_i - \tfrac{2}{3}\pi R^3$$

$$= \sum_{i=1}^{L} \pi \left[R^2 - \left(R - \sum_{j=1}^{i} h_i \right)^2 \right] h_i - \tfrac{2}{3}\pi R^3. \qquad (1)$$

We could apply the Lagrange multiplier method to solve the problem in which we may construct an auxiliary function

$$F(h_1, h_2, \ldots, h_L) = E(h_1, h_2, \ldots, h_L) + \lambda \varphi(h_1, h_2, \ldots, h_L) \qquad (2)$$

with the condition function $\varphi(h_1, h_2, \ldots, h_L) = 0$, where

$$\varphi(h_1, h_2, \ldots, h_L) = (h_1 + h_2 + \cdots + h_L - R) = 0 \qquad (3)$$

and λ is a constant. By calculating the partial differential of $h_1, h_2, \ldots, h_L$, and letting them equal 0, we have the partial differential equations set (4). Finally, we can find the values of $h_1, h_2, \ldots, h_L$ by solving the partial differential equations set (4).

$$\begin{aligned}
&\frac{\partial F(h_1, h_2, \ldots, h_L)}{\partial h_1} = \frac{\partial E(h_1, h_2, \ldots, h_L)}{\partial h_1} + \lambda \frac{\partial \varphi(h_1, h_2, \ldots, h_L)}{\partial h_1} = 0 \\
&\frac{\partial F(h_1, h_2, \ldots, h_L)}{\partial h_2} = \frac{\partial E(h_1, h_2, \ldots, h_L)}{\partial h_2} + \lambda \frac{\partial \varphi(h_1, h_2, \ldots, h_L)}{\partial h_2} = 0 \\
&\vdots \\
&\frac{\partial F(h_1, h_2, \ldots, h_L)}{\partial h_L} = \frac{\partial E(h_1, h_2, \ldots, h_L)}{\partial h_L} + \lambda \frac{\partial \varphi(h_1, h_2, \ldots, h_L)}{\partial h_L} = 0 \\
&\varphi(h_1, h_2, \ldots, h_L) = h_1 + h_2 + \cdots + h_L - R = 0.
\end{aligned} \qquad (4)$$

For example, we may find $h_1 = \boldsymbol{R}/3, h_2 = 2\boldsymbol{R}/3$ when $\boldsymbol{L} = 2$, and $h_1 = 0.1623\boldsymbol{R}$, $h_2 = 0.1821\boldsymbol{R}$, $h_3 = 0.2185\boldsymbol{R}$, $h_4 = 0.4371\boldsymbol{R}$ when $\boldsymbol{L} = 4$, etc. When $\boldsymbol{L}$ is large enough, the volume error may be neglected. In particular, the volume error $E(h_1, h_2, \ldots, h_L)$ is less than 4.59% of the volume of the hemisphere when $\boldsymbol{L} = 16$ and $E(h_1, h_2, \ldots, h_L)$ is less than 2.32% of the volume of the hemisphere when $\boldsymbol{L} = 32$.

To analyse the antireflective properties of the multi-level structure shown in figure 2, we could take each level as a single step columned grid structure shown in figure 3 and apply boundary conditions between the levels. As Zhang [21] has already analysed the characteristics of the single-step columned grid grating, we may follow his program in the calculations of each level.

For the lth layer shown in figure 3, the space is divided into three regions labelled by regions I, II and III. In regions I and III, the light field may be written in terms of plane-wave expansions. Let $\boldsymbol{E}^{\mathrm{i}}$ be the incident field with wavevector k_1 and a polarization vector $\boldsymbol{u}$, $\boldsymbol{R}_{mn}$ be the reflected waves with wavevector k_{1mn} in region I and T_{mn} be the transmitted waves with wavevector k_{3mn} in region III, respectively. According to the Rayleigh expansions, the electric fields may be represented by

$$\boldsymbol{E}^{\mathrm{I}} = \boldsymbol{E}^{\mathrm{i}} + \sum_{m=-\infty}^{\infty} \sum_{n=-\infty}^{\infty} \boldsymbol{R}_{mn} \times \exp(\mathrm{i}\boldsymbol{k}_{1mn} \times \boldsymbol{r}) \qquad (5)$$

$$\boldsymbol{E}^{\mathrm{III}} = \sum_{m=-\infty}^{\infty} \sum_{n=-\infty}^{\infty} \boldsymbol{T}_{mn} \times \exp[\mathrm{i}\boldsymbol{k}_{3mn} \times (\boldsymbol{r} - \boldsymbol{h})]. \qquad (6)$$

In region II, let $\boldsymbol{E}^{\mathrm{II}}$ and $\boldsymbol{H}^{\mathrm{II}}$ be the electric and magnetic fields, respectively. Their components can each be written as an expansion in terms of a particular set of the space harmonics, which are approximated to be independent of z as follows:

$$\boldsymbol{E}^{\mathrm{II}} = \sum_{m=-\infty}^{\infty} \sum_{n=-\infty}^{\infty} [E_{mn}^{x}(z)\boldsymbol{i} + E_{mn}^{y}(z)\boldsymbol{j}] \times \exp[\mathrm{i}(k_{xm}\boldsymbol{i} + k_{yn}\boldsymbol{j})] \qquad (7)$$

$$\boldsymbol{H}^{\mathrm{II}} = \left(\frac{\varepsilon_0}{\mu_0}\right)^{-1/2} \sum_{m=-\infty}^{\infty} \sum_{n=-\infty}^{\infty} [H_{mn}^{x}(z)\boldsymbol{i} + H_{mn}^{y}(z)\boldsymbol{j}] \times \exp[\mathrm{i}(k_{xm}\boldsymbol{i} + k_{yn}\boldsymbol{j})]. \qquad (8)$$

In the following, we rewrite the permittivity ϵ and its reciprocal ϵ^{-1} of the grating by the Fourier expansion

$$\epsilon(x, y, z) = \sum_{p=-\infty}^{\infty} \sum_{q=-\infty}^{\infty} \epsilon_{pq}(z) \times \exp\left[\mathrm{i}\left(p\frac{2\pi}{T_x}x + q\frac{2\pi}{T_y}y\right)\right] \qquad (9)$$

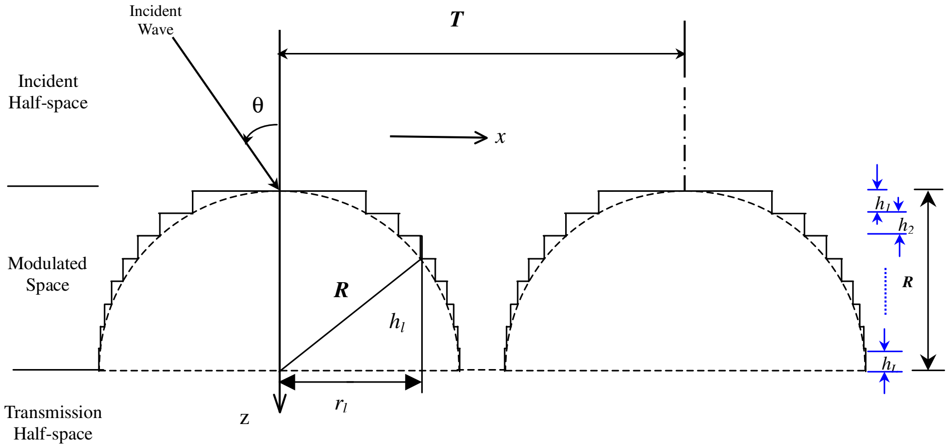

Figure 2. Geometry of the multi-step column structure and the hemispherical grad grating.

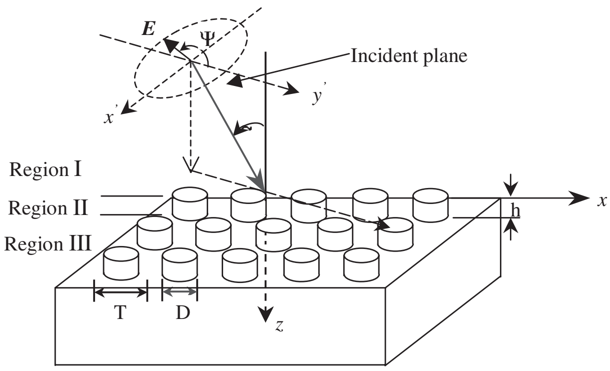

Figure 3. Geometry of the 2D columned grid grating diffraction problem analysed.

$$\epsilon^{-1}(x, y, z) = \sum_{p=-\infty}^{\infty} \sum_{q=-\infty}^{\infty} \bar{\epsilon}_{pq}(z) \times \exp\left[\mathrm{i}\left(p\frac{2\pi}{T_x}x + q\frac{2\pi}{T_y}y\right)\right] \tag{10}$$

respectively, with

$$\epsilon_{pq}(z) = \frac{1}{T_x T_y} \int_{-\frac{T_x}{2}}^{\frac{T_x}{2}} \int_{-\frac{T_y}{2}}^{\frac{T_y}{2}} \epsilon \times \exp\left[-\mathrm{i}\left(p\frac{2\pi}{T_x}x + q\frac{2\pi}{T_y}y\right)\right] \mathrm{d}x\,\mathrm{d}y \tag{11}$$

$$\bar{\epsilon}_{pq}(z) = \frac{1}{T_x T_y} \int_{-\frac{T_x}{2}}^{\frac{T_x}{2}} \int_{-\frac{T_y}{2}}^{\frac{T_y}{2}} \frac{1}{\epsilon} \times \exp\left[-\mathrm{i}\left(p\frac{2\pi}{T_x}x + q\frac{2\pi}{T_y}y\right)\right] \mathrm{d}x\,\mathrm{d}y. \tag{12}$$

For the lth columned grid grating, the permittivity is expressed as

$$\epsilon_l = \begin{cases} \epsilon_1 & -T_x/2 < x < T_x/2, \quad -T_y/2 < y < T_y/2, \\ & \text{and} \quad x^2 + y^2 > r_l^2 \\ \epsilon_2 & x^2 + y^2 < r_l^2 \end{cases} \tag{13}$$

with subscript $l = 1, \ldots, \boldsymbol{L}$ denoting levels (layers) l.

Here, we use the inverse of Toeplitz matrix presented by Li [22] to improve the convergence of the coupled-wave method.

To solve the electric and magnetic fields in reign II, Moharam and Gaylord [23] used a state-variable method, which gives the solution to be written in terms of the eigenvalues and eigenvectors of the corresponding coefficient matrix

$$E^x_{mn} = \sum_j C_j \phi^1_{mn,j} \exp(r_j z) \tag{14}$$

$$E^y_{mn} = \sum_j C_j \phi^2_{mn,j} \exp(r_j z) \tag{15}$$

$$H^x_{mn} = \sum_j C_j \phi^3_{mn,j} \exp(r_j z) \tag{16}$$

$$H^y_{mn} = \sum_j C_j \phi^4_{mn,j} \exp(r_j z) \tag{17}$$

with the eigenvalues r_j and the elements $\phi^l_{mn,j}$ of the eigenvector matrix. By substituting equations (10)–(13) into the group of Maxwell's differential equation, we obtain the following characteristic equation

$$\boldsymbol{r}\boldsymbol{\phi} = \boldsymbol{\phi}\boldsymbol{A} \tag{18}$$

where $\boldsymbol{A}$ is a constant matrix. After determination of matrix $\boldsymbol{A}$, we find r_j and $\phi^l_{mn,j}$ by solving the eigenvalues and eigenvectors of $\boldsymbol{A}$. Then we consider the electromagnetic boundary conditions and calculate the constant coefficients C_j left as unknown in equations (10)–(13). The next step of the procedure is to determine the components of $\boldsymbol{R}_{mn}$ and $\boldsymbol{T}_{mn}$, which are calculated via equations (10)–(13) and the electromagnetic boundary conditions.

To fulfil the boundary conditions between the two levels as the following

$$E^x_{mn,l}(h_l) = E^x_{mn,l+1}(h_l), \tag{19}$$

$$E^y_{mn,l}(h_l) = E^y_{mn,l+1}(h_l), \tag{20}$$

$$H^x_{mn,l}(h_l) = H^x_{mn,l+1}(h_l), \tag{21}$$

$$H^y_{mn,l}(h_l) = H^y_{mn,l+1}(h_l), \tag{22}$$

with $l = 1, 2, \ldots, L$ denoting the coordinate of each level at the boundary, we have the relation

$$\begin{aligned} A_1(h)C_1 &= A_2(h)C_2 \\ A_2(2h)C_2 &= A_3(2h)C_3 \\ &\vdots \\ A_l(lh)C_l &= A_l + l(lh)C_{l+1} \\ &\vdots \end{aligned} \tag{23}$$

So we can give the expression

$$C_1 = A_1'(h)A_2(h)A_2'(2h)A_3(2h)\cdots A_{l-1}'(lh-h)A_l(lh)C_l \tag{24}$$

where $\boldsymbol{A}_l$ is the lth level coefficient matrix and $\boldsymbol{C}_l$ denotes the expansion coefficient matrix of the lth level field expression. Due to this relation, we could calculate $\boldsymbol{C}_l$ via $\boldsymbol{A}_1, \ldots, \boldsymbol{A}_l$ and $\boldsymbol{C}_1$.

The diffraction efficiencies η_{mn}^{I} and η_{mn}^{III} for the reflected and transmitted waves may be given by

$$\eta_{mn}^{\mathrm{I}} = \mathrm{Re}(k_{zmn}^{\mathrm{I}}/k_{z00}^{\mathrm{I}})|R_{mn}|^2 \tag{25}$$

and

$$\eta_{mn}^{\mathrm{III}} = \mathrm{Re}(k_{zmn}^{\mathrm{III}}/k_{z00}^{\mathrm{III}})|T_{mn}|^2 \tag{26}$$

where Re denotes the real part of a variable, and k_{zmn}^{I} and k_{zmn}^{III} are the components along the z-direction of the wavevectors k_{1mn} and k_{3mn}, respectively. For a lossless grating in which the permittivity ϵ^{III} is a real number, conservation of energy requires that

$$\sum_{m=-\infty}^{\infty}\sum_{n=-\infty}^{\infty}(\eta_{mn}^{\mathrm{I}} + \eta_{mn}^{\mathrm{III}}) = 1. \tag{27}$$

3. Results and discussion

With the formulae above, we could study the characteristics of the multi-level stairstep surface-relief grating, and the programs were written in Matlab language V6.5. When the total number of the steps $\boldsymbol{L}$ is large enough ($\boldsymbol{L} \geqslant 8$), the multi-step structure may approximate the surface-relief grating with hemispherical grid with very little error. In our program we use a 16-step structure to approximate the hemispherical grid surface-relief grating. In this paper, we use some basic parameter as below, the refractive indices of the grating $n_s = 1.5$, the refractive indices of the surrounding media $n_i = 1$ and the number of the stairs $\boldsymbol{L} = 16$.

As a hemispherical grid grating, it has two important structure parameters, the period $\boldsymbol{T}$ and diameter $\boldsymbol{D}$. Figure 4 shows the relation between reflectivity and the period of the hemisphere, with parameters: wavelength $\lambda = 0.6$ μm, $\boldsymbol{D} = 0.8\boldsymbol{T}$, incident angle $\alpha = 0°$ and polarization angle $\Psi = 90°$. We can see that the reflectivity is below 0.2% when the period is between 0.35 and 0.6 μm. Moreover, the reflectivity approximates 0 when the period approximates 0.39 μm. Therefore, we can design the grating with the period between 0.35 and 0.6 μm to achieve good antireflective properties. If we design to fabricate a hemispherical grating

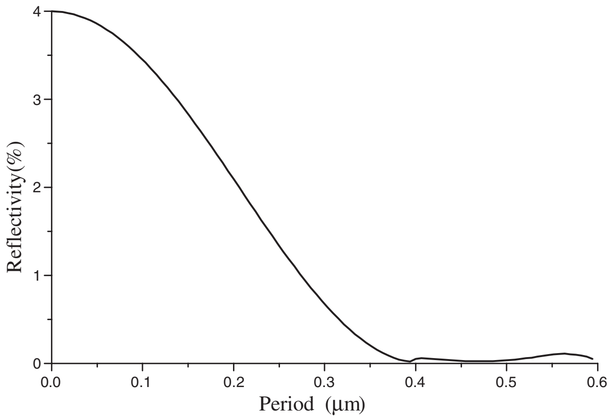

Figure 4. Relation between reflectivity and the period of the hemisphere, with parameters: wavelength $\lambda = 0.6$ μm, $\boldsymbol{D} = 0.8\boldsymbol{T}$, $\Psi = 90°$ and $\alpha = 0°$.

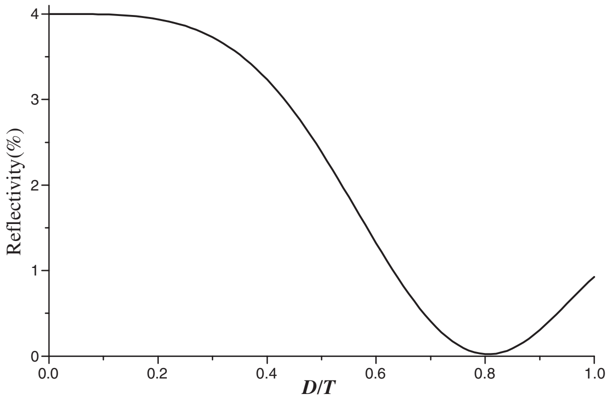

Figure 5. Relation between reflectivity and $\boldsymbol{D}/\boldsymbol{T}$, with parameters: $\boldsymbol{T} = 0.39$ μm, wavelength $\lambda = 0.6$ μm, $\Psi = 90°$ and $\alpha = 0°$.

with the period of 0.475 μm, the fabrication error within ± 0.125 μm (26.3% error) could have very little effect on the antireflective properties of this kind of grating.

Figure 5 presents the relation between reflectivity and the value $\boldsymbol{D}/\boldsymbol{T}$, with parameters $\boldsymbol{T} = 0.39$ μm and wavelength $\lambda = 0.6$ μm. We can see that the value $\boldsymbol{D}/\boldsymbol{T}$ has great influence on the reflectivity. When it is below 0.53, the reflectivity is above 2% and only when it approximates 0.8 can the reflectivity approximate 0. Compared with figure 4, we may find that controlling the value $\boldsymbol{D}/\boldsymbol{T}$ precisely is a very important problem when we fabricate this kind of grating. To get good antireflective characteristics, we should make $\boldsymbol{D}$ equal $0.8\boldsymbol{T}$ and the fabrication errors should not be larger than $0.11\boldsymbol{T}$ (± 0.04 μm) if we want reflectivity to be less than 0.5%; this result could be realized by modern chemical technology.

Figure 6 shows the reflectivity curves for this kind of grating in the visible waveband at normal incidence. We can see that the grating can achieve extremely low reflection, which is below 0.3%, to cover the whole visible light waveband. This property shows that this kind of grating is very useful to reduce the reflectance of visible light.

Figures 7 and 8 present the reflectivity curves for this kind of grating in the visible waveband at normal incidence when we adopt different slicing methods, and we can see the influence of the total number of the stairs $\boldsymbol{L}$ on our results. Comparing the two figures, we may find that the convergency is accelerated

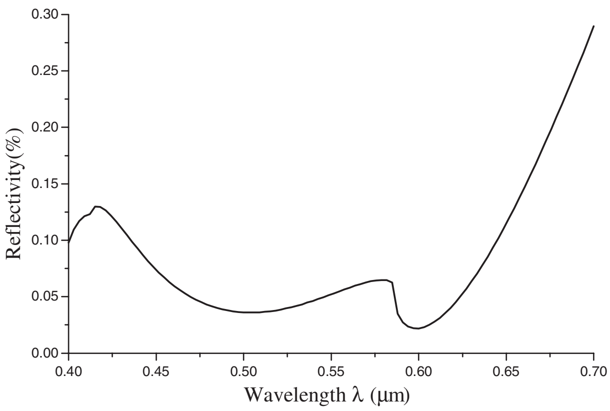

Figure 6. Diagram of reflectivity in the visible waveband, with parameters: $T = 0.39\ \mu$m, $\boldsymbol{D} = 0.8\boldsymbol{T}$, $\Psi = 90°$ and $\alpha = 0°$.

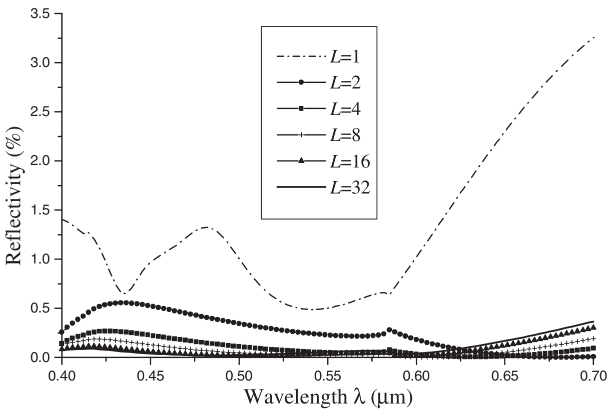

Figure 7. Diagram of reflectivity in the visible waveband with $\boldsymbol{L}$ being equal to 1, 2, 4, 8, 16 and 32, with parameters: $\boldsymbol{T} = 0.39\ \mu$m, $\boldsymbol{D} = 0.8\boldsymbol{T}$, $\Psi = 90°$ and $\alpha = 0°$, where the height of the slices $h_1, h_2, \ldots, h_L$ are the results of the Lagrange multiplier method.

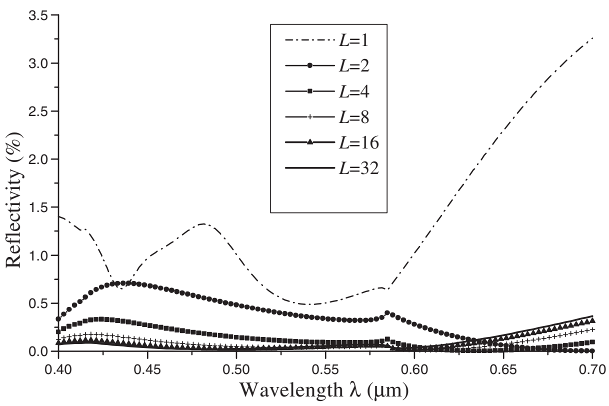

Figure 8. Diagram of reflectivity in the visible waveband with $\boldsymbol{L}$ being equal to 1, 2, 4, 8, 16 and 32, with parameters: $\boldsymbol{T} = 0.39\ \mu$m, $\boldsymbol{D} = 0.8\boldsymbol{T}$, $\Psi = 90°$ and $\alpha = 0°$, where the height of the slices $h_1, h_2, \ldots, h_L$ are equal to each other.

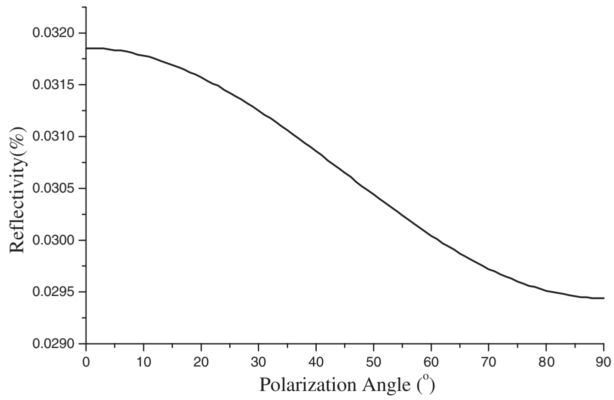

Figure 9. Relation between reflectivity and polarization angle, with parameters: $\boldsymbol{T} = 0.39\ \mu$m, $\lambda = 0.6\ \mu$m, $\boldsymbol{D} = 0.8\boldsymbol{T}$ and $\alpha = 10°$.

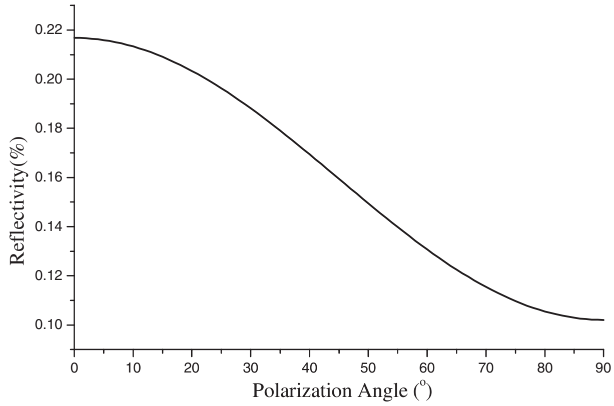

Figure 10. Relation between reflectivity and polarization angle, with parameters: $\boldsymbol{T} = 0.39\ \mu$m, $\lambda = 0.6\ \mu$m, $\boldsymbol{D} = 0.8\boldsymbol{T}$ and $\alpha = 20°$.

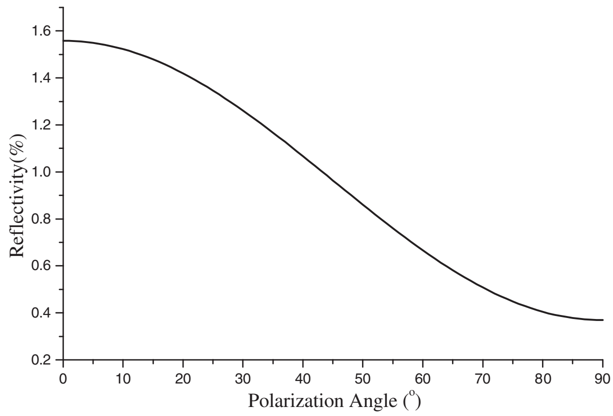

Figure 11. Relation between reflectivity and polarization angle, with parameters: $\boldsymbol{T} = 0.39\ \mu$m, $\lambda = 0.6\ \mu$m, $\boldsymbol{D} = 0.8\boldsymbol{T}$ and $\alpha = 30°$.

by adopting the Lagrange multiplier method and the errors are also obviously lessened when $\boldsymbol{L} \leqslant 8$. However, we can see that the errors become neglectable when $\boldsymbol{L}$ is large enough ($\boldsymbol{L} \geqslant 16$) and we can hardly distinguish the difference between the two curves corresponding to $\boldsymbol{L} = 16$ (volume error less than 4.59%) and $\boldsymbol{L} = 32$ (volume error less than 2.32%) in both figures 7 and 8. We can also see from the two figures that the effect of the Lagrange multiplier method becomes weak when $\boldsymbol{L}$ increases (especially when $\boldsymbol{L} \geqslant 16$). So the results in this paper with the 16-level structure are very credible.

Due to the symmetry of the problem, we can know that when the polarization angle of the incident wave is varied from

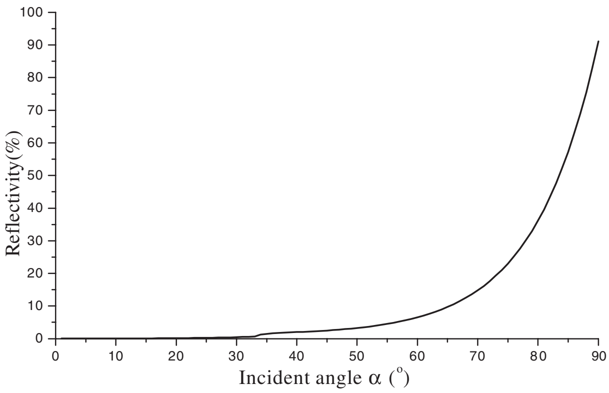

Figure 12. Relation of reflectivity versus incident angle, with parameters: $T = 0.39\ \mu$m, $\lambda = 0.6\ \mu$m, $\Psi = 90°$ and $D = 0.8T$.

0° to 90° there is hardly any change in the reflectivity in the case of normal incidence ($\alpha = 0°$). Then, figures 9–11 show the dependence of reflection on polarization angle in the case of non-normal incidence ($\alpha = 10°, 20°, 30°$). It can be seen from the three figures that the reflectivity decreases when the polarization angle increases from 0° to 90°. Moreover, the reflectivity decreases more rapidly with the same increment of the polarization angle when α is larger.

The relation of reflectivity versus incident angle α is shown in figure 12. We can see that the hemispherical grid grating can achieve extremely low reflectivity over the very wide field of incidence. We can get very low reflectance which is less than 0.5% over the field of view larger than 60°.

4. Summary and conclusions

In this paper, the algorithm of coupled-wave analysis for a two-dimensional surface-relief grating with hemispherical grid is studied and the results of our computer simulation for the grating are presented. By computer simulation, we obtained the relations between the reflectivity and the various grating parameters. Fortunately, the results satisfy energy conservation, and the numerical instability problem and the convergence problem have not emerged in our calculations.

We find that this kind of grating can be designed over the whole visible light waveband and it can achieve extremely low reflectance over a broad field of view, which will be very useful when designing a novel optical system.

References

[1] Grann E B, Moharam M G and Pommet D A 1995 Optimal design for antireflective tapered two-dimensional subwavelength grating structures *J. Opt. Soc. Am.* **12** 333–9

[2] Grann E B, Moharam M G and Pommet D A 1994 Artificial uniaxial and biaxial dielectrics with use of two-dimensional subwavelength binary gratings *J. Opt. Soc. Am.* A **11** 2695–703

[3] Motamedi M E, Southwell W H and Gunning W J 1990 Antireflection surface in silicon using binary optics technology *Appl. Opt.* **31** 4372–6

[4] Gaylord T K, Baird W E and Moharam M G 1986 Zero-reflectivity high spatial-frequency rectangular-groove dielectric surface-relief gratings *Appl. Opt.* **25** 4562–7

[5] Gaylord T K, Glytsis E N and Moharam M G 1987 Zero-reflectivity homogeneous layers and high spatial-frequency surface-relief gratings on lossy materials *Appl. Opt.* **26** 3123–35

[6] Raguin D H and Morris G M 1993 Antireflection structured surfaces for the infrared spectral region *Appl. Opt.* **32** 1154–67

[7] Urquhart K S, Stein R and Lee S H 1995 Computer-generated holograms fabricated by direct write of positive electron-beam resist *Opt. Lett.* **18** 308–10

[8] Schindler A *et al* 2001 Ion beam and plasma jet etching for optical component fabrication *Proc. SPIE* **4440** 217–27

[9] Malek C K, Hartley F T and Neogi J 2000 Focused ion beam direct micromachining of DOEs *Proc. SPIE* **4075** 167–72

[10] Schnabel B and Kley E-B 1997 Fabrication and application of subwavelength gratings *Proc. SPIE* **3008** 233–41

[11] Kanamori Y, Sasaki M and Hane K 1999 High-aspect-ratio two-dimensional silicon subwavelength gratings fabricated by fast atom beam etching *Proc. SPIE* **3874** 345–54

[12] Lalanne P and Morris G M 1996 Design, fabrication, and characterization of subwavelength periodic structures for semiconductor antireflection coating in the visible domain *Proc. SPIE* **2776** 300–9

[13] Kuzmenko P J, Ciarlo D R and Stevens C G 1994 Fabrication and testing of a silicon immersion grating for infrared spectroscopy *Proc. SPIE* **2266** 566–77

[14] Wiedemann G R, Dave H H and Jennings D E 1993 Immersion grating and etched gratings for infrared astronomy *Proc. SPIE* **1946** 622–8

[15] Kawamura K, Sarukura N, Hirano M and Hosono H 2000 Fabrication of non-erasable gratings in SiO_2 glasses by a two-beam holographic method using infrared femtosecond laser pulses *Proc. SPIE* **4347** 195–206

[16] Pool F S, Wilson D W, Maker P D, Muller R E, Gill J J, Sengupta D K, Liu J K, Bandara S V and Gunapala S D 1998 Fabrication and performance of diffractive optics for quantum well infrared photodetectors *Proc. SPIE* **3379** 402–9

[17] Xia Y, Gates B, Yin Y and Yu Lu 2000 Monodispersed colloidal spheres: old materials with new applications *Adv. Mater.* **12** 693–713

[18] Sprenger M, Walheim S, Schafle C and Steiner U 2003 Hierarchical pattern replication by polymer demixing *Adv. Mater.* **15** 703–6

[19] Xia Y, Tien J, Qin D and Whitesides G M 1996 Non-photolithographic methods for fabrication of elastomeric stemps for use in microcontact printing *Langmuir* **12** 4033–8

[20] Hirai T and Hayashi S 1999 Lens functions of polymer microparticle arrays *Colloids Surf.* A **153** 503–13

[21] Zhang D, Lu Z, Yu W and Li F 2002 Electromagnetic diffraction analysis of columned grid gratings *J. Opt. A: Pure Appl. Opt.* **4** 180–6

[22] Li L 1996 Use of Fourier series in the analysis of discontinuous periodic structures *J. Opt. Soc. Am.* A **13** 1870–6

[23] Moharam M G and Gaylord T K 1983 Three-dimensional vector coupled-wave analysis of planar-grating diffraction *J. Opt. Soc. Am.* **73** 1105–12